photonics

MDPI

Article

Dual-Degree-of-Freedom Continuous Optical Zoom Endoscopic System Based on Liquid Lenses

Qiheng Wei [1,†], Yongqiang Zhang [1,†], Lingyuan Wu [1], Yuhan Huang [2], Yanglong Li [1], Bo Fu [1], Wei Li [1,*] and Zhao Jiang [3,*]

[1] Institute of Fluid Physics, China Academy of Engineering Physics, Mianyang 621900, China; weiqiheng@caep.cn (Q.W.); zhangyongqiang@caep.cn (Y.Z.); wuly@caep.cn (L.W.); liyanglong@caep.cn (Y.L.); fubo@caep.cn (B.F.)
[2] School of Nursing, Fudan University, Shanghai 200032, China; 23111170005@m.fudan.edu.cn
[3] School of Remote Sensing Science and Technology, Aerospace Information Technology University, Jinan 250200, China
* Correspondence: liwei1994@caep.cn (W.L.); jiangzhao@aitech.edu.cn (Z.J.)
† These authors contributed equally to this work.

Abstract

Endoscopic imaging plays an important role in minimally invasive surgery, clinical diagnosis, and biomedical research. Conventional endoscopic systems with fixed focal lengths are limited in multi-scale observation, while mechanically driven zoom systems often suffer from increased structural complexity and limited stability. In this work, a dual-degree-of-freedom continuous optical zoom endoscopic system based on liquid lenses is proposed. By employing two independently tunable liquid lenses, the system enables simultaneous modulation of optical power and principal plane position, thereby enhancing the flexibility of continuous focusing and magnification control. A Gaussian-bracket-based model is established to describe optical power redistribution and aberration evolution during the zoom process. The proposed system achieves continuous focusing over a wide range from 10 mm to 1000 mm while maintaining imaging performance close to the diffraction limit. In addition, a 1.2× magnified state is realized at a short focusing distance without significant degradation in image quality. The results demonstrate that the proposed dual-degree-of-freedom design provides a compact and effective solution for high-resolution continuous zoom endoscopic imaging.

Keywords: liquid lenses; endoscopic imaging; continuous optical zoom; Gaussian bracket method; optical system design

Check for updates

Received: 22 April 2026
Revised: 14 May 2026
Accepted: 26 May 2026
Published: 27 May 2026

Copyright: © 2026 by the authors. Licensee MDPI, Basel, Switzerland. This article is an open access article distributed under the terms and conditions of the Creative Commons Attribution (CC BY) license.

1. Introduction

Endoscopic imaging is a fundamental technique in modern medical diagnostics and minimally invasive interventions, playing a key role in Minimally Invasive Surgery, clinical diagnosis, and biomedical research [1–4]. To meet the demand for observing tissues at different depths and scales, endoscopic systems are expected to provide zoom capability. However, conventional endoscopes are typically designed with fixed focal lengths, which limits their adaptability. Although mechanical zoom systems have been developed, they inevitably increase system complexity and size and often suffer from slow responses and limited stability [5–7].

In recent years, liquid lenses have attracted significant attention due to their compact structure, low power consumption, and fast response [8–14]. Liquid lenses enable

continuous focal length tuning without mechanical movement, offering high flexibility in optical system design. Owing to these advantages, liquid lenses have been widely applied in various display and imaging systems, including cameras [15–18], microscopy [19–25], and telescope [26–30], where fast and adaptive focusing is required.

In endoscopic imaging, the introduction of liquid lenses provides additional benefits [31–36], such as eliminating mechanical motion, reducing system complexity, and enabling rapid focal adjustment within confined spaces. These features make liquid lenses particularly suitable for miniaturized and high-speed endoscopic systems. However, existing liquid-lens-based endoscopic systems still face limitations [37], including a restricted focusing range and relatively large system size, which hinder their application in wide-range and high-resolution imaging scenarios.

In this paper, a dual-degree-of-freedom continuous optical zoom endoscope based on liquid lenses is proposed. By employing two independently tunable liquid lenses, the system enables simultaneous modulation of optical power and principal plane position, thereby enhancing the flexibility of continuous focusing and magnification control. The system achieves continuous focal length tuning by modulating the liquid interface curvature, and a zoom model is established using the Gaussian bracket method to analyze optical power distribution. A compact optical structure is designed and evaluated at different focal states. The results demonstrate that the system maintains high imaging quality over a focusing distance ranging from 10 mm to 1000 mm, with the modulation transfer function approaching the diffraction limit.

2. Operating and Design Principle

2.1. Zoom Principle of Elastomer Liquid Lens

The core of the continuous zoom endoscopic system lies in the adaptive focusing capability of the elastomeric liquid lens. In the proposed system, the liquid lenses acts as the only tunable optical element, enabling continuous zoom through electrically induced interface deformation, while the solid lenses are used to correct aberrations and improve imaging quality.

Unlike electrowetting-based liquid lenses, the liquid lens used in this work operates based on an elastomeric actuation mechanism. Its structure typically consists of a sealed cavity, a transparent elastic membrane, and driving electrodes. When a voltage is applied, the electric field induces deformation of the elastic membrane, thereby modifying the curvature of the liquid interface and adjusting the optical power. This mechanism provides advantages such as fast response, high optical axis stability, and no mechanical wear.

Under the paraxial approximation, the optical power of the liquid lens can be expressed as [38]:

$$\Phi_L(V) = \frac{n_{eff} - n_0}{R(V)}, \tag{1}$$

where n_{eff} is the effective refractive index of the liquid lens, n_0 is the refractive index of the surrounding medium, and $R(V)$ is the voltage-dependent radius of curvature.

For elastomeric liquid lenses, the curvature variation is governed by membrane deformation under the electric field. It can be approximated that the curvature follows a nonlinear relationship with the applied voltage [39]:

$$\frac{1}{R(V)} = k_1 V + k_2 V^2, \tag{2}$$

where k_1 and k_2 are system-dependent coefficients related to membrane stiffness, actuator configuration, and liquid volume constraints. The optical power can be expressed as

$$\Phi_L(V) = (n_{eff} - n_0)(k_1 V + k_2 V^2), \tag{3}$$

which indicates that the optical power varies nonlinearly with the applied voltage, and its tuning range is determined by the elastomeric structure and actuation mechanism.

According to device characteristics, the optical power of the liquid lens can be continuously tuned over a wide range (e.g., from negative to positive optical power), corresponding to a continuous change in focal length from far to near distances. Compared with conventional mechanically driven focusing systems, this approach enables fast response, stable field of view, and high repeatability. Therefore, by adjusting the driving voltage V, a continuous mapping from voltage to curvature, optical power, and system focal length can be established, providing the physical foundation for mechanically free continuous optical zoom.

2.2. Principle of System Zoom

To quantitatively describe the mechanism of continuous focusing and magnification control in the dual-liquid-lens system, the Gaussian bracket method is employed for first-order paraxial modeling. The system consists of two elastomeric liquid lenses and six solid lenses. Along the optical axis, the optical powers are denoted as φ_1, φ_2, φ_{L1}, φ_3, φ_{L2}, φ_4, φ_5, and φ_6 and the normalized separations as e_1, e_2, e_3, e_4, e_5, e_6, and e_7. The total optical power is expressed as

$$\Phi = [\varphi_1, -e_1, \varphi_2, -e_2, \varphi_{L1}, -e_3, \varphi_3, -e_4, \varphi_{L2}, -e_5, \varphi_4, -e_6, \varphi_5, -e_7, \varphi_6]. \tag{4}$$

where φ_1–φ_6 denote the optical powers of the solid lenses, φ_{L1} and φ_{L2} represent the optical powers of the two liquid lenses, and e_1–e_7 denote the normalized separations between adjacent optical elements along the optical axis. The Gaussian bracket [ ] represents the first-order paraxial system power calculation.

Since only the liquid lenses are tunable, expanding φ_{L1} and φ_{L2} yields

$$\Phi = a_{11}\varphi_{L1}\varphi_{L2} + a_{10}\varphi_{L1} + a_{01}\varphi_{L2} + a_{00}, \tag{5}$$

where a_{11}, a_{10}, a_{01}, and a_{00} are constant coefficients determined by the fixed solid-lens structure. Compared with single liquid lens systems, the dual liquid lenses configuration introduces additional degrees of freedom, enabling simultaneous control of optical power and principal plane positions.

The optical power of each liquid lens depends on the driving voltage, the total optical power becomes

$$\Phi(V_1, V_2) = a_{11}\varphi_{L1}(V_1)\varphi_{L2}(V_2) + a_{10}\varphi_{L1}(V_1) + a_{01}\varphi_{L2}(V_2) + a_{00}. \tag{6}$$

where φ_{L1} (V_1) and φ_{L2} (V_2) denote the voltage dependent optical powers of the two liquid lenses.

Based on first-order Gaussian optics [38], with a fixed image plane, the object-side focusing distance can be expressed as

$$FD(V_1, V_2) = \frac{1}{\frac{1}{l'} - \Phi(V_1, V_2)}, \tag{7}$$

indicating that the focusing position is fully determined by the driving states of the two liquid lenses.

Considering the principal-plane shifts in the thick optical system [36], the lateral magnification can be expressed as

$$\beta(V_1, V_2) = -\frac{l' - H'(V_1, V_2)}{WD(V_1, V_2) - H(V_1, V_2)}, \tag{8}$$

where l' denotes the image distance between the rear principal plane to the image plane, $H(V_1,V_2)$ and $H'(V_1,V_2)$ denote the positions of the principal planes. Since the dual-liquid-lens system simultaneously modulates both the total optical power and the principal plane positions, it enables unified control of focusing and magnification.

In summary, the dual-liquid-lens system provides bilinear tunability of the total optical power and enables continuous focusing and magnification variation through coordinated control of optical power and principal plane positions.

3. Design Results

3.1. Zoom Lens Design Results

To verify the feasibility of the proposed continuous optical zoom endoscopic system, optical modeling and optimization are performed. The system consists of six solid lenses and two elastomeric liquid lenses, forming a compact zoom structure without mechanical movement.

The solid lenses are used to correct spherical aberration, chromatic aberration, and field curvature, while the liquid lenses act as the tunable elements for continuous focusing and magnification control. The dual liquid lens configuration provides two degrees of freedom, enabling simultaneous modulation of optical power and principal plane position, which is essential for large range focusing and near field magnification enhancement. The liquid lenses used in this work are commercially available elastomeric liquid lenses, featuring ultra-fast response (<1 ms), high optical-axis stability, and low power consumption (<1 mW). The useful aperture is approximately 1.55 mm on the sensor side, and the focal length can be tuned over a wide range (approximately $(-\infty, -50\text{ mm}) \cup (6.25\text{ mm}, +\infty)$), enabling effective and continuous focal modulation.

Based on these characteristics, the optical power distribution and aberration correction are jointly optimized using the solid lenses, while the liquid lenses extend the focusing range. The optimization step is performed at wavelengths of 0.486 μm, 0.587 μm, and 0.656 μm. A merit function incorporating multi-field performance and variable optical power constraints is constructed to optimize the system parameters and liquid lens states. The detailed optical parameters of the proposed system, including the radii of curvature, thicknesses, materials, and spacing, are summarized in Table 1.

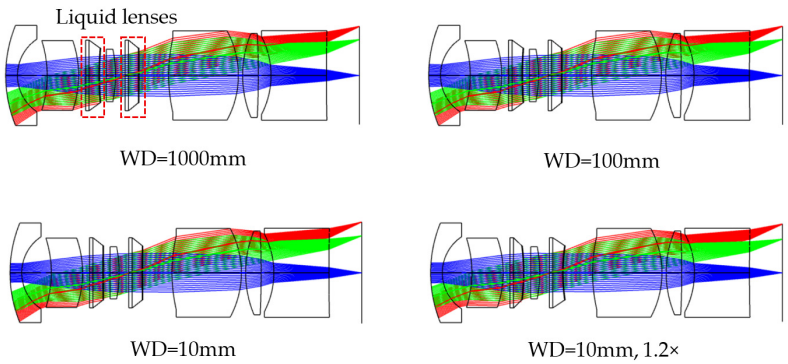


Figure 1. Layout results of the zoom endoscopic system. Red represents the full field of view, green represents the 0.75 field of view, and blue represents the zero field of view.

Table 1. Optical system parameters of the zoom endoscopic system.

	Surface Type	Radius	Thickness	Material	Semi-Diameter
0	Object	Infinity	10.000		8.104
1		3.750	0.334	LAKL21	1.419
2		1.234	0.844		1.027
3		−3.234	0.892	N-LAK33B	0.987
4		−2.992	0.196		0.976
5		Infinity	0.100	BK7	0.775
6	Polymer	Infinity	0.280	Index Nd: 1.57 Abbe Vd: 30.0	0.775
7	Membrane	−6.319	0.020	Index Nd: 1.53 Abbe Vd: 65.4	0.775
8		−6.319	0.190		0.775
9		406.922	0.258	N-PSK53A	0.741
10		−3.817	0.273		0.711
11	Stop	Infinity	0.000		0.574
12		Infinity	0.100	BK7	0.775
13	Polymer	Infinity	0.280	Index Nd: 1.57 Abbe Vd: 30.0	0.775
14	Membrane	5.395	0.020	Index Nd: 1.53 Abbe Vd: 65.4	0.775
15		5.395	0.837		0.775
16		4.667	1.978	SK6	1.056
17		−2.660	0.121		1.264
18		3.092	0.443	BSM16	1.193
19		−26.414	0.363		1.155
20		−2.389	1.570	S-NPH3	1.110
21		58.351	0.936		1.267
22	Image	Infinity	-		1.393

The final optimized layout is shown in Figure 1. The proposed system achieves continuous focusing over a wide focusing distance range from 10 mm to 1000 mm and enables a 1.2× magnified state. The design also achieves a wide field of view of 80° within a compact size of 10 mm in length and 3 mm in diameter.

3.2. Image Quality Analysis

The proposed zoom endoscopic system is designed and evaluated to characterize its optical performance, as shown in Figure 2. The modulation transfer function (MTF) is analyzed at focusing distances of 1000 mm, 100 mm, and 10 mm, together with the 1.2× magnified state at 10 mm. The MTF curves are calculated in Zemax OpticStudio 2024R1 using the polychromatic FFT MTF analysis at the image plane under different focusing states. The MTF is evaluated at three wavelengths (0.486 µm, 0.587 µm, and 0.656 µm), with the diffraction-limited curve as a reference.

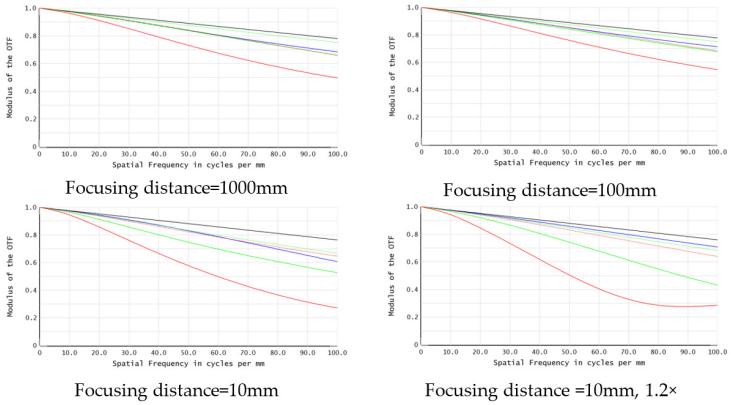


Figure 2. Modulation Transfer Function of the zoom endoscopic system. Red represents the full field of view, green represents the 0.75 field of view, and blue represents the zero field of view. The solid and dashed lines denote the meridional and sagittal planes, respectively. The black line indicates the diffraction limit.

At focusing distances of 1000 mm and 100 mm, the MTF remains close to the diffraction limit over most spatial frequencies, reaching approximately 0.5 when the spatial frequency exceeds 100 lp/mm, indicating good contrast transfer capability. Only slight degradation is observed at high spatial frequencies, mainly in the off-axis field, demonstrating stable imaging performance during continuous refocusing. At 10 mm, the high-frequency MTF decreases due to increased sensitivity to residual aberrations and field curvature but still reaches approximately 0.3 above 100 lp/mm, indicating a preserved high-frequency response. In the 1.2× magnified state at 10 mm, the MTF is slightly reduced, especially in the off-axis field, due to optical power redistribution and increased aberration sensitivity introduced by dual-liquid-lens modulation. Nevertheless, the overall performance remains high, demonstrating that magnification is achieved without significant loss of image quality.

The polychromatic PSF distributions of the proposed system are analyzed at the image plane under focusing distances of 1000 mm, 100 mm, and 10 mm, as well as at the 1.2× magnified state at 10 mm, as shown in Figure 3. In all cases, the PSF exhibits a pronounced central peak with concentrated energy, indicating good focusing performance. At 1000 mm and 100 mm, the PSF remains compact and well confined, which is consistent with the high MTF at corresponding spatial frequencies. At 10 mm, the PSF slightly broadens due to increased aberration sensitivity, corresponding to the reduced high-frequency MTF; however, the energy remains mainly concentrated in the central region, indicating stable imaging performance under short focusing distance conditions. In the 1.2× magnified state at 10 mm, the PSF shows a slight additional broadening, but the central peak remains well defined, demonstrating that the system maintains good focusing capability despite increased aberration sensitivity.

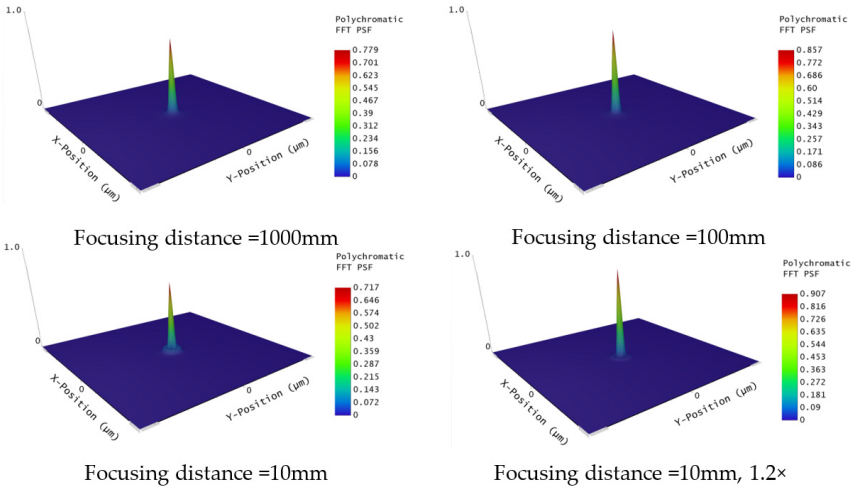


Figure 3. Point Spread Function of the zoom endoscopic system.

The spot diagrams of the proposed system are evaluated at different focusing distances and at the 1.2× magnified state at 10 mm, as shown in Figure 4. The RMS spot radii of all fields are smaller than or comparable to the Airy disk radius, indicating performance approaching the diffraction limit. At 1000 mm, the spot distributions are compact and nearly symmetric, while at 100 mm and 10 mm, the spot size slightly increases with elongation in off-axis fields due to residual astigmatism and coma during large-range focusing. In the 1.2× magnified state at 10 mm, the spot distribution becomes slightly larger, especially at the edge field, caused by optical-power redistribution and principal plane variation induced by dual-liquid-lens tuning. In addition, the limited aperture of the liquid lenses restricts marginal rays at large field angles, leading to some degradation in edge-field performance; however, the overall spot distribution remains well controlled, indicating effective aberration balancing across the field.

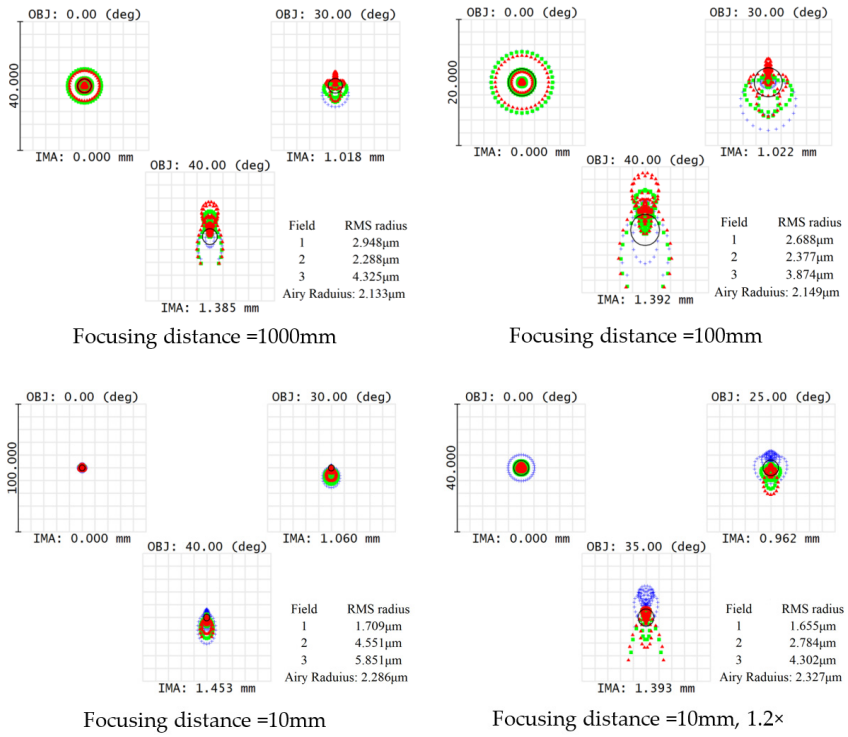


Figure 4. Spot Diagrams of the zoom endoscopic system. Red represents the full field of view, green represents the 0.75 field of view, and blue represents the zero field of view.

To further investigate the aberration evolution under different focusing states, the ray fan distributions of the proposed system are analyzed, as shown in Figure 5. At the focusing distances of 1000 mm and 100 mm, the ray fan curves remain relatively compact and symmetric over most fields, indicating well-balanced aberration correction and stable imaging performance. Only slight residual spherical aberration and field-dependent distortion are observed, while the tangential and sagittal ray deviations remain relatively small.

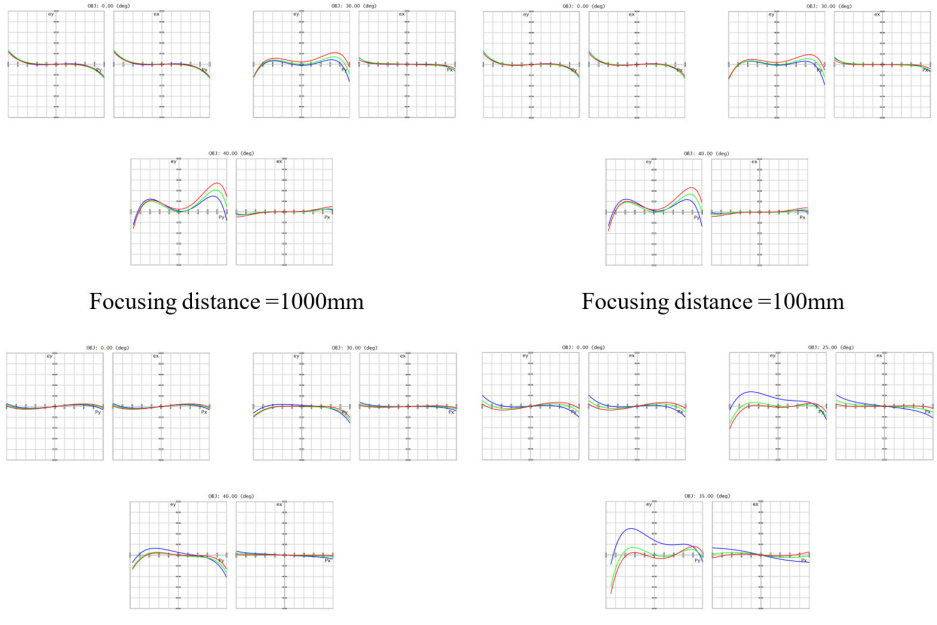


Figure 5. Ray fan of the zoom endoscopic system. Red represents the full field of view, green represents the 0.75 field of view, and blue represents the zero field of view.

As the focusing distance decreases to 10 mm, the off-axis ray fan gradually expands, particularly in the tangential direction, indicating increased sensitivity to residual aberrations such as coma, astigmatism, and field curvature caused by the optical-power redistribution of the dual-liquid-lens system. Compared with the long-focus states, the edge-field ray deviation becomes more noticeable due to the larger optical power required under short focusing-distance conditions. In the 1.2× magnified state at 10 mm, the edge-field ray fan exhibits slightly stronger asymmetry and larger deviation, especially at large field angles. This phenomenon mainly results from the simultaneous modulation of optical power and principal-plane position, which enhances the coupling between off-axis aberrations and field-angle variation. In addition, the limited effective aperture of the elastomeric liquid lenses partially restricts marginal rays, leading to slightly increased edge-field aberration accumulation. Nevertheless, the overall ray fan distributions remain relatively smooth and well controlled, demonstrating stable aberration balancing and good imaging quality throughout the continuous focusing range.

Figure 6 shows the simulated colonic endoscopic images at four states: 1000 mm, 100 mm, 10 mm, and the 1.2× magnified state at 10 mm. The simulated images are generated in Zemax OpticStudio using the image simulation module based on the optimized optical system under different focusing states, where the corresponding polychromatic PSF, diffraction effects, residual aberrations, and magnification variations are considered to reproduce the final imaging performance on the image plane. The simulations are performed under a consistent field height of 49 mm, and the imaging performance is evaluated in terms of resolution and aberration characteristics.

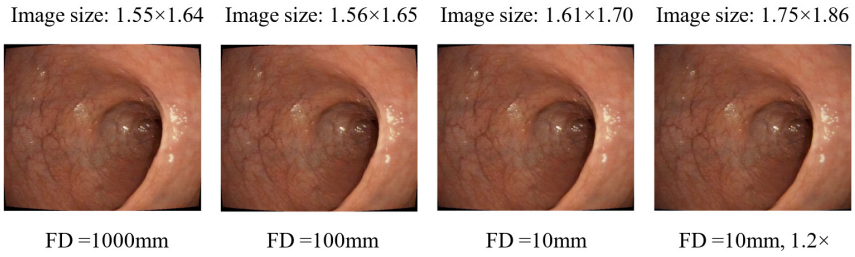


Figure 6. Image Simulation of the zoom endoscopic system.

At 1000 mm, the image appears relatively less sharp, with lower contrast and less distinct high-frequency features, mainly due to defocus and field-dependent aberrations. As the focusing distance decreases to 100 mm and further to 10 mm, the image sharpness and contrast gradually improve. At 10 mm, the image exhibits higher sharpness and improved contrast. At the 1.2× magnified state at 10 mm, the system achieves the best visual performance, with clearer fine structures and higher contrast. In the simulated images, the apparent reduction in the visual impact of aberrations at shorter focusing distances mainly arises from the increased magnification under a fixed field height, which enlarges the image scale on the sensor and reduces the visual perception of aberration-induced distortions. Meanwhile, the 1.2× magnified state further enlarges the image scale, making high-frequency structures more distinguishable and resulting in better perceived image quality. This also explains the difference between the image simulation results and the MTF-based frequency-domain evaluation. Although slight edge distortion remains, overall aberrations are well controlled.

Overall, the simulation results indicate that the proposed system maintains high imaging quality throughout the entire focusing range, with consistent and stable visual performance under different focusing and magnification states.

4. Tolerance Analysis

To evaluate the robustness of the proposed continuous optical zoom endoscopic system, a tolerance analysis was performed considering realistic manufacturing and assembly errors, including surface form, thickness, refractive-index variations, and element misalignments. The tolerances were defined at the micrometer level, with a decenter of ±0.01–0.02 mm, a tilt of ±0.05°, and a refractive-index variation of ±0.0005. A Monte Carlo approach with a normal distribution was employed, and 200 trials were performed to evaluate the combined effects of all tolerances across multiple focusing states, including 1000 mm, 100 mm, 10 mm, and the 1.2× magnified condition.

The MTF distributions shown in Figure 7, where each colored curve represents one Monte Carlo trial under the corresponding focusing condition, indicate that most tolerance-perturbed systems remain close to the nominal performance, particularly at long and intermediate focusing distances. The spread of the MTF curves is relatively limited in low- and mid-spatial frequencies, demonstrating stable contrast transfer under typical conditions. As the focusing distance decreases to 10 mm and under the 1.2× magnified state, increased dispersion is observed, mainly due to higher sensitivity to residual aberrations and alignment errors. Nevertheless, no severe degradation or performance failure is observed.

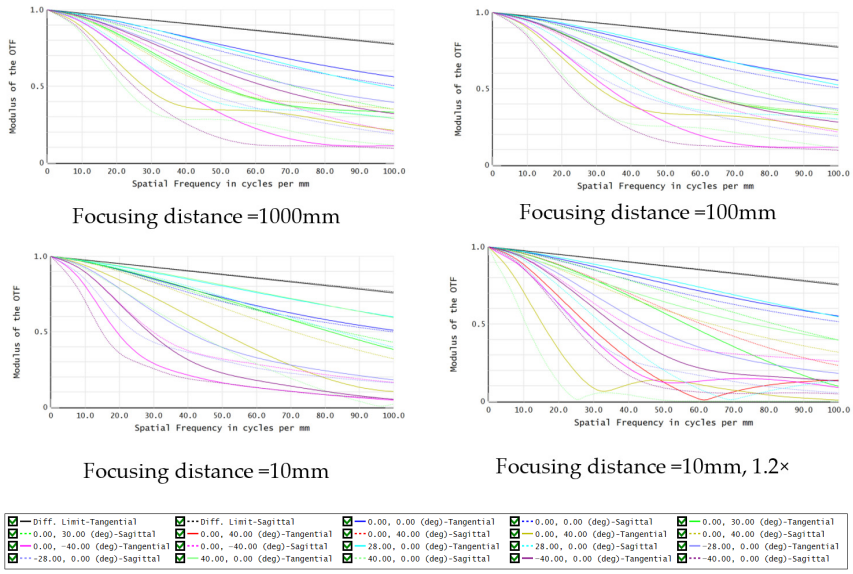


Figure 7. MTF curve of Monte Carlo Analysis.

In conclusion, the results confirm that the proposed system maintains stable imaging performance over the entire focusing range and exhibits strong robustness against manufacturing and assembly errors, indicating good feasibility for practical implementation.

5. Discussion

The paraxial model in this work is not only used to analyze the dual-degree-of-freedom continuous zoom mechanism, but also serves as the basis for generating the initial structure of the detailed Zemax optical system. According to the system requirements, the operating wavelengths were first determined as 0.486 μm, 0.587 μm, and 0.656 μm, with a total system length of approximately 10 mm and a maximum outer diameter of about 3 mm. The system was designed to achieve a continuous focusing range from 10 mm to 1000 mm while providing approximately 1.2× magnification at the 10 mm near focus state with a fixed image plane position. Based on Gaussian optics and paraxial imaging theory, Equations (1)–(3) were first used to calculate the voltage-dependent optical powers of the two elastomeric liquid lenses under different driving voltages (V_1 and V_2). Subsequently,

Equations (4)–(6) were employed to derive the equivalent optical power distribution of the entire optical system using the Gaussian bracket method. Based on the obtained system optical power, Equation (7) was used to determine the object-side focusing distance under different driving states, while Equation (8) was further used to calculate the magnification and principal-plane shifts.

Based on these first-order optical parameters, including the image distance, lens spacing, and principal-plane distribution, the initial Zemax sequential configuration was established by assigning the initial curvatures of the two liquid lenses, the optical-power distribution of the six solid lenses, the element spacing, the aperture-stop position, and the fixed image-plane location. After generating the initial structure, the six solid lenses were further optimized to correct spherical aberration, coma, astigmatism, and field curvature while preserving the dual-degree-of-freedom continuous focusing and zoom capability provided by the two liquid lenses. Therefore, the paraxial model in this work is not only used for theoretical analysis, but also directly participates in the generation of the initial practical optical structure, providing physical constraints and parameter initializations for the subsequent Zemax optimization process, thereby improving the optimization efficiency and practical realizability of the proposed system.

The visual differences among the simulated images in Figure 6 remain relatively limited because the proposed system maintains consistently high imaging performance over all focusing states. As shown by the MTF analysis, the MTF curves under different focusing distances remain relatively close to each other, particularly in the central field region and low-to-middle spatial-frequency ranges, resulting in similar overall visual quality in the simulated images. The primary performance differences mainly appear in the edge-field regions, where the 1000 mm focusing state exhibits relatively stronger field-dependent aberrations and distortion. In addition, the image simulations are based on natural colonic endoscopic images containing relatively smooth and repetitive tissue textures, making high-frequency differences less visually distinguishable to the human eye.

To further clarify the differences between the proposed system and previously reported liquid-lens-based endoscopic systems, a comparison is summarized in Table 2. The proposed system employs two independently tunable elastomeric liquid lenses, enabling simultaneous modulation of optical power and principal-plane position. Compared with previously reported systems, the proposed design demonstrates advantages in focusing range, compactness, response speed, and continuous magnification capability, indicating its potential for compact high-resolution continuous zoom endoscopic imaging.

Table 2. Comparison of the proposed endoscope and endoscopes.

Reference	Zoom Ratio	Focusing Distance	Response Time	Volume
[34]	4×	-	-	ø 4 mm × *L* 23.26 mm
[35]	-	10 mm~100 mm	<7.5 ms	ø 34 mm × *L* 48.5 mm
[36]	-	20 mm~200 mm	<2 ms	ø 38 mm × *L* 20 mm
This work	1.2×	10 mm~1000 mm	<1 ms	ø 3 mm × *L* 10 mm

In the 1.2× magnified state, slight degradation of the edge-field imaging performance is observed compared with the normal focusing states. This phenomenon mainly arises from the stronger optical-power redistribution and principal-plane shifts introduced by the dual-liquid-lens modulation under the magnified condition. As the magnification increases, the off-axis field becomes more sensitive to residual aberrations such as astigmatism, coma, and field curvature. In addition, the limited effective aperture of the elastomeric liquid lenses partially restricts marginal rays at large field angles, resulting in increased aberration accumulation in the edge field. Nevertheless, the central field still maintains compact PSF distributions and relatively high MTF performance, while the overall spot distributions

remain close to the Airy disk radius. Therefore, although slight edge field degradation exists in the 1.2× magnified state, the overall imaging quality remains stable and acceptable for continuous zoom endoscopic imaging applications.

6. Conclusions

In this paper, a dual-degree-of-freedom continuous optical zoom endoscopic system based on liquid lenses is proposed. By employing two independently tunable liquid lenses, the system achieves coordinated modulation of optical power and principal plane position, enabling simultaneous continuous focusing and magnification control. A Gaussian-bracket-based first-order model is established to guide the optical design and optimization process. The proposed system realizes continuous focusing from 1000 mm to 10 mm and achieves a 1.2× magnified state at a short focusing distance while maintaining imaging performance close to the diffraction limit. Simulation results demonstrate stable imaging quality across different focusing states, and tolerance analysis based on 200 Monte Carlo trials further verifies the robustness and feasibility of the system under practical manufacturing and assembly conditions. The proposed approach provides a compact, mechanically free, and effective solution for continuous zoom endoscopic imaging.

Author Contributions: Conceptualization, Q.W. and Y.H.; methodology, Q.W. and Y.H.; software, Q.W. and L.W.; validation, Q.W., Y.H. and L.W.; formal analysis, Y.H. and Y.L.; investigation, B.F. and Y.L.; resources, Y.Z., W.L. and Z.J.; data curation, Q.W. and L.W.; writing—original draft preparation, Q.W. and Y.H.; writing—review and editing, Y.Z., W.L. and Z.J.; visualization, Y.H. and B.F.; supervision, Y.Z., W.L. and Z.J.; project administration, Y.Z., W.L. and Z.J.; funding acquisition, Y.Z., W.L. and Z.J. All authors have read and agreed to the published version of the manuscript.

Funding: This research was funded by Presidential Foundation of CAEP, grant number YZJJZL2025008, National Key Laboratory on Advanced Laser and High Power Microwave, grant number LMLB202404002, project ZR2025QC1601 supported by Shandong Provincial Natural Science Foundation and Research Initiation Project for High-Level Talent Team of Aerospace Information Technology University (No. 301010202).

Data Availability Statement: All data generated or analyzed during this study are included in this published article.

Acknowledgments: We acknowledge the support from the Major Program of Basic Science and Technology Research for National Defense.

Conflicts of Interest: The authors declare no conflicts of interest.

References

1. Tang, Y.; Anandasabapathy, S.; Richards-Kortum, R. Advances in optical gastrointestinal endoscopy: A technical review. *Mol. Oncol.* **2021**, *15*, 2580–2599. [CrossRef]
2. Kim, D.; Chang, S.; Kwon, H.S. Wide field-of-view, high-resolution plastic lens design with low F-number for disposable endoscopy. *Photonics* **2021**, *8*, 89. [CrossRef]
3. Boese, A.; Wex, C.; Croner, R.; Liehr, U.B.; Wendler, J.J.; Weigt, J.; Walles, T.; Vorwerk, U.; Lohmann, C.H.; Friebe, M.; et al. Endoscopic imaging technology today. *Diagnostics* **2022**, *12*, 1262. [CrossRef]
4. Cai, Q.; Deng, R.; Pan, Y.; Liu, R.; Chen, Y.; Gong, G.; Zou, J.; Yang, H.; Han, D. Robotic wireless capsule endoscopy: Recent advances and upcoming technologies. *Nat. Commun.* **2024**, *15*, 4597. [CrossRef]
5. Zou, Y.; Zhang, W.; Chau, F.S.; Zhou, G. Miniature adjustable-focus endoscope with a solid electrically tunable lens. *Opt. Express* **2015**, *23*, 20582–20592. [CrossRef]
6. Zou, Y.; Chau, F.S.; Zhou, G. Ultra-compact optical zoom endoscope using solid tunable lenses. *Opt. Express* **2017**, *25*, 20675–20688. [CrossRef] [PubMed]
7. Sun, W.S.; Tien, C.L.; Chen, P.Y. Cost-effective design of a miniaturized zoom lens for a capsule endoscope. *Micromachines* **2022**, *13*, 1814. [CrossRef] [PubMed]

8. Dong, L.; Agarwal, A.; Beebe, D.J.; Jiang, H.J. Adaptive liquid microlenses activated by stimuli-responsive hydrogels. *Nature* **2006**, *442*, 551–554. [CrossRef]
9. López, C.; Hirsa, A. Fast focusing using a pinned-contact oscillating liquid lens. *Nat. Photonics* **2008**, *2*, 610–613. [CrossRef]
10. Xu, J.B.; Zhao, Y.R.; Yuan, R.Y.; Li, X.W.; Liu, C.; Wang, Q.H. Electrowetting liquid lens integrating adaptive liquid iris. *Opt. Laser Technol.* **2024**, *169*, 110023. [CrossRef]
11. Zhao, Y.R.; Li, Z.S.; Zheng, Y.; Wang, D.; Lu, X.K.; Lin, Y.C.; Zhang, H.R.; Liu, C.; Wang, Q.H. Non-aqueous electrowetting liquid lens with centimeter-level large aperture based on dielectric failure suppression principle. *Light Sci. Appl.* **2025**, *14*, 120. [CrossRef] [PubMed]
12. Liu, C.; Zheng, Y.; Wang, D.; Huang, Q.; Li, X.W.; Lin, F.C.; Zhao, Y.R.; Zheng, Y.W.; Lu, X.K.; Li, X.R.; et al. Multi-wavelength achromatic 3D meta-holography with zoom function. *Adv. Sci.* **2025**, *12*, 2501881. [CrossRef]
13. Tian, L.L.; Hu, W.; Zhou, H.Z.; Yu, L.; Li, L.; Li, L. SRGAN algorithm-assisted electrically controllable zoom system based on Pancharatnam-Berry liquid crystal lens for VR/AR display. *ACS Photonics* **2024**, *11*, 2787–2796. [CrossRef]
14. Cui, Z.B.; Pan, J.T.; Tao, X.Y.; Hu, J.S.; Hou, G.P.; Zhang, Z.C.; Ye, M.; Zhou, X.Y.; Lu, Y.Q.; Chai, Z.; et al. High-efficiency liquid-crystal polarization metalens for chip-scale atomic magnetometers. *Laser Photonics Rev.* **2026**, *20*, e02517. [CrossRef]
15. Wang, D.; Liu, C.; Shen, C.; Xing, Y.; Wang, Q.H. Holographic capture and projection system of real object based on tunable zoom lens. *PhotoniX* **2020**, *1*, 6. [CrossRef]
16. Wang, D.; Li, Z.S.; Zheng, Y.; Zhao, Y.R.; Liu, C.; Xu, J.B.; Zheng, Y.W.; Huang, Q.; Chang, C.L.; Zhang, D.W.; et al. Liquid lens based holographic camera for real 3D scene hologram acquisition using end-to-end physical model-driven network. *Light Sci. Appl.* **2024**, *13*, 62. [CrossRef]
17. Zheng, Y.; Zhang, H.R.; Li, X.W.; Zhao, Y.R.; Li, Z.S.; Hou, Y.H.; Liu, C.; Wang, Q.H. Fast-zoom and high-resolution sparse compound-eye camera based on dual-end collaborative optimization. *Opto-Electron. Adv.* **2025**, *8*, 240285. [CrossRef]
18. Li, Z.S.; Liu, C.; Li, X.W.; Zheng, Y.; Huang, Q.; Zheng, Y.W.; Hou, Y.H.; Chang, C.L.; Zhang, D.W.; Zhuang, S.L.; et al. Real-time holographic camera for obtaining real 3D scene hologram. *Light Sci. Appl.* **2025**, *14*, 74. [CrossRef] [PubMed]
19. Jiang, Z.; Wang, D.; Zheng, Y.; Liu, C.; Wang, Q.H. Continuous optical zoom microscopy imaging system based on liquid lenses. *Opt. Express* **2021**, *29*, 20322–20335. [CrossRef]
20. Liu, C.; Jiang, Z.; Wang, X.; Zheng, Y.; Zheng, Y.W.; Wang, Q.H. Continuous optical zoom microscope with extended depth of field and 3D reconstruction. *PhotoniX* **2022**, *3*, 20. [CrossRef]
21. Yuan, R.Y.; Ma, X.L.; Zheng, Y.; Jiang, Z.; Wang, X.; Liu, C.; Wang, Q.H. 3D microscope image acquisition method based on zoom objective. *Opt. Express* **2023**, *31*, 16067–16080. [CrossRef] [PubMed]
22. Guo, C.L.; Blair, G.J.; Sehgal, M.; Jimka, F.N.S.; Bellafard, A.; Silva, A.J.; Golshani, P.; Basso, M.A.; Blair, H.T.; Aharoni, D. Miniscope-LFOV: A large-field-of-view, single-cell-resolution miniature microscope for imaging neural dynamics. *Sci. Adv.* **2023**, *9*, eadg3918. [CrossRef] [PubMed]
23. Zheng, Y.; Wang, X.; Jiang, Z.; Xu, J.B.; Yuan, R.Y.; Zhao, Y.R.; Zhang, H.R.; Liu, C.; Wang, Q.H. Adaptive multiscale microscope with fast zooming, extended working distance, and large field of view. *Light Adv. Manuf.* **2024**, *5*, 62–74. [CrossRef]
24. Shi, R.H.; Chen, X.Y.; Deng, J.H.; Liang, J.H.; Fan, K.K.; Zhou, F.F.; Tang, P.F.; Zhang, L.C.; Kong, L.J. Random-access wide-field mesoscopy for centimetre-scale imaging of biodynamics with subcellular resolution. *Nat. Photonics* **2024**, *18*, 721–730. [CrossRef]
25. Yu, D.X.; Jiang, Z.; Zheng, Y.; Zhang, H.R.; Li, R.Q.; Zhao, Y.R.; Lu, X.K.; Lin, Y.C.; Liu, C.; Wang, Q.H. Large zoom ratio and adaptive aberration correction microscope using 4DPSF-aware physical degradation-guided network. *Light Sci. Appl.* **2026**, *15*, 140. [CrossRef]
26. Lin, Y.H.; Chen, M.S.; Lin, H.C. An electrically tunable optical zoom system using two composite liquid crystal lenses with a large zoom ratio. *Opt. Express* **2011**, *19*, 4714–4721. [CrossRef]
27. Li, L.; Wang, D.; Liu, C.; Wang, Q.H. Ultrathin zoom telescopic objective. *Opt. Express* **2016**, *24*, 18674–18684. [CrossRef]
28. Liu, Z.; Hong, H.; Gan, Z.; Chen, Y.; Xing, K. Flexible zoom telescopic optical system design based on genetic algorithm. *Photonics* **2022**, *9*, 536. [CrossRef]
29. He, Z.; Yin, K.; Wu, S.T. Miniature planar telescopes for efficient, wide-angle, high-precision beam steering. *Light Sci. Appl.* **2021**, *10*, 134. [CrossRef] [PubMed]
30. Jiang, Z.; Zheng, Y.; Wang, X.; Zhao, Y.R.; Yuan, R.Y.; Liu, C.; Wang, Q.H. Continuous optical zoom telescopic system based on liquid lenses. *Opt. Express* **2024**, *32*, 15269–15279. [CrossRef]
31. Seo, S.W.; Han, S.; Seo, J.H.; Kim, Y.M.; Kang, M.S.; Min, N.K. Microelectromechanical-system-based variable-focus liquid lens for capsule endoscopes. *Jpn. J. Appl. Phys.* **2009**, *48*, 337–354. [CrossRef]
32. Seo, S.W.; Han, S.; Seo, J.H.; Choi, W.B.; Sung, M.Y. Liquid lens module with wide field-of-view and variable focal length. *Electron. Mater. Lett.* **2010**, *6*, 141–144. [CrossRef]
33. Zeng, X.; Smith, C.T.; Gould, J.C.; Heise, C.P.; Jiang, H. Fiber endoscopes utilizing liquid tunable-focus microlenses actuated through infrared light. *J. Microelectromech. Syst.* **2011**, *20*, 583–593. [CrossRef]

34. Lee, S.; Choi, M.; Lee, E.; Jung, K.D.; Chang, J.H.; Kim, W. Zoom lens design using liquid lens for laparoscope. *Opt. Express* **2013**, *21*, 1751. [CrossRef]
35. Volpi, D.; Tullis, I.D.C.; Barber, P.R.; Augustyniak, E.M.; Vojnovic, B. Electrically tunable fluidic lens imaging system for laparoscopic fluorescence-guided surgery. *Biomed. Opt. Express* **2017**, *8*, 3232–3247. [CrossRef] [PubMed]
36. Liu, C.; Zheng, Y.; Li, N.N.; Hou, Y.H.; Jiang, Z.; Wang, Q.H. Real scene acquisition and holographic near-eye display system based on a zoom industrial endoscope. *Opt. Express* **2022**, *30*, 33170–33181. [CrossRef]
37. Liu, C.; Zheng, Y.; Yuan, R.Y.; Jiang, Z.; Xu, J.B.; Zhao, Y.R.; Wang, X.; Li, X.W.; Xing, Y.; Wang, Q.H. Tunable liquid lenses: Emerging technologies and future perspectives. *Laser Photonics Rev.* **2023**, *17*, 2300274. [CrossRef]
38. Hecht, E. *Optics*, 5th ed.; Pearson: London, UK, 2017.
39. Ren, H.; Wu, S.T. Tunable-focus liquid lens controlled using an electrically activated membrane. *Opt. Express* **2007**, *15*, 5931–5936. [CrossRef]

Disclaimer/Publisher's Note: The statements, opinions and data contained in all publications are solely those of the individual author(s) and contributor(s) and not of MDPI and/or the editor(s). MDPI and/or the editor(s) disclaim responsibility for any injury to people or property resulting from any ideas, methods, instructions or products referred to in the content.